UNIVERSITYOF BIRMINGHAM

Volcanism and wildfire associated with deep-time deglaciation during the Artinskian (early Permian)

Wang, Ye; Lu, Jing; Yang, Minfang; Yager, Joyce; Greene, Sarah; Sun, Ruoyu; Mu, Xiaomiao; Bian, Xiao; Zhang, Peixin; Shao, Longyi; Hilton, Jason

Link to publication on Research at Birmingham portal

Volcanism and wildfire associated with deep-time deglaciation during the Artinskian (early Permian)

Ye Wang [a], Jing Lu [a,**], Minfang Yang [b], Joyce A. Yager [c,d], Sarah E. Greene [d], Ruoyu Sun [e], Xiaomiao Mu [e], Xiao Bian [a], Peixin Zhang [a], Longyi Shao [a], Jason Hilton [d,f,*]

[a] State Key Laboratory of Coal Resources and Safe Mining, College of Geoscience and Surveying Engineering, China University of Mining and Technology, Beijing 100083, PR China
[b] Petroleum Exploration and Development Research Institute, PetroChina, Beijing 100083, PR China
[c] University of Southern California, Department of Earth Sciences, United States of America
[d] School of Geography, Earth and Environmental Sciences, University of Birmingham, Edgbaston, Birmingham B15 2TT, UK
[e] Institute of Surface-Earth System Science, School of Earth System Science, Tianjin University, 300072 Tianjin, China
[f] Birmingham Institute of Forest Research, University of Birmingham, Edgbaston, Birmingham B15 2TT, UK

ARTICLE INFO

ABSTRACT

The deep-time geological record can provide insights into the processes and mechanisms of glacier retreat. Ice sheets of the Late Paleozoic Ice Age (LPIA) collapsed extensively during the early Artinskian (early Permian) approximately 290 million years ago through massive glacial melting that was associated with dramatic increases in global temperature, atmospheric pCO$_2$, sea level, and resulted in profound changes in terrestrial plant distribution and diversity. A hypothesized mode of this extensively glacial melting is multiple large-scale volcanic events, but the causes and effects have not yet been clearly established because of the lack of detailed coeval records of volcanism and environmental changes. Here, we present a record of these events from an Artinskian terrestrial succession in the Liujiang Coalfield, North China. Our new U-Pb zircon dating, high-resolution chemostratigraphy, and kerogen maceral data reveal that environmental changes (carbon cycle perturbation, wildfire, and continental weathering) in the region were intricately linked with the large-scale volcanism associated with the Tarim-II, Panjal and Choiyoi volcanic provinces. Our study shows that hypothesized volcanism and wildfire raised temperatures by releasing greenhouse gases, while the ensuing warming led to ice sheet melting, the release of terrestrial Hg and C and resulting Hg and C cycle anomalies.

1. Introduction

The Late Paleozoic Ice Age (LPIA; ca. 360–254.5 Ma) was the longest ice house period of the Phanerozoic and represents an important window for understanding the co-evolution of terrestrial climate, environment, and biota as ice sheets repeatedly advanced and retreated across mid–high latitude Gondwana (Montañez et al., 2007; Poulsen et al., 2007; Goddéris et al., 2017; Richey et al., 2020; Lu et al., 2021c; Fielding et al., 2023). Within the LPIA, eastern and western Australia, Antarctica, Saudi Arabia, India, and eastern South America transitioned into non-glacial conditions during the early Artinskian stage (e.g., Isbell et al., 2003; Montañez and Poulsen, 2013; Fielding et al., 2023 and references therein), here defined as the Artinskian deglaciation (AD). The AD

bounds the P1 and P2 glaciations (Fielding et al., 2008) with deglaciation commencing in the earliest Artinskian and ending by the mid-Artinskian (Fielding et al., 2023). Accompanying these changes were significant global climatic and environmental shifts, including a dramatic increase in sea level (Fielding et al., 2008), global temperature (Yang et al., 2014), and atmospheric pCO$_2$ (Montañez et al., 2007; Poulsen et al., 2007; Richey et al., 2020), changes to continental weathering regimes (e.g., Yang et al., 2014; Scheffler et al., 2006), and a decline of peat-forming (coal) forest area (Cleal and Thomas, 2005). At present, the driving mechanism for this deglaciation event was attributed to the global warming via the release of greenhouse gases (e.g., Ernst and Youbi, 2017).

Mercury contents and isotope ratios in sediments have been widely

---

Fig. 1. Location and geological context for the study area. a, Cisuralian paleogeography highlighting the position of the North China Plate and the Liujiang Coalfield, global igneous centers and key study locations (base map from Scotese, 2014). b, Map of the North China Plate showing location of the Liujiang Coalfield and sedimentary environments of the Shanxi Formation (modified from Shang, 1999). c, Stratigraphic framework and sedimentology of the studied succession from Wang, 2010. Age of #D from Lu et al. (2021a). Abbreviations: St. stratigraphy; F. – Formation; L. – Lopingian; C. – Capitanian; S. – Shiqianfeng; Litho. - Lithofacies; Asse. – Asselian; Sak. – Sakmarian; m. Mos. – middle Moscovian; Gzh. – Gzhelian. # denotes numbered coal seams.

used to trace and evaluate the record of volcanism in geological history, and to determine Hg source(s) and evaluate Hg's transport mechanisms in the Earth system (e.g., Sanei et al., 2012; Grasby et al., 2019; Shen et al., 2020a; Percival et al., 2021; Yager et al., 2021; Shen et al., 2022a). Volcanism and wildfires are the main causes of abnormal mercury enrichment anomalies in strata (Shen et al., 2020a, 2020b; Shen et al., 2022). Volcanism can not only release Hg directly into the atmosphere, but can also lead to abnormal Hg accumulation in sediments through magma heating of organic-rich sediments (e.g., Shen et al., 2020b; Shen et al., 2022). Meanwhile, burning (caused by wildfire) of surface organic matter and soil erosion can also cause Hg enrichment anomalies (Blum et al., 2014; Thibodeau et al., 2016; Shen et al., 2020b; Shen et al., 2022), because the majority (>90%) of Hg in terrestrial systems resides in soils and is associated with organic matter (e.g., Shen et al., 2020b; Shen et al., 2022).

Photochemically-induced Hg mass independent fractionation (MIF) can effectively trace the source and pathway of Hg in various environments (Blum et al., 2014; Sun et al., 2020; Shen et al., 2020b). The gaseous Hg directly released from volcanism usually has near-zero MIF values. In contrast, the positive MIF of gaseous oxidized Hg is imparted into marine systems (including sediments and organisms) via wet deposition. The photochemical reactions in the atmosphere associated with Hg oxidation in both airborne water droplets and surface waters

also can produce positive MIF (Blum et al., 2014). However, in terrestrial environments, plants absorb atmospheric gaseous mercury through their stomata, resulting in negative MIF in their photosynthetic organs (e.g., leaves and stems) (Blum et al., 2014). These processes tend to produce negative MIF in continental systems (including coal, soil, sediments, and plants) (e.g., Blum et al., 2014). During LIP events, volcanogenic Hg may dominate total Hg input in sediments, resulting in near-zero MIF (Thibodeau et al., 2016; Them et al., 2019; Shen et al., 2022a), or negative MIF through magma heating of organic-rich sediments and enhanced soil erosion (Them et al., 2019; Shen et al., 2020b; Shen et al., 2022a).

In this study, we document the links between the Artinskian environmental changes and volcanism and wildfire for the first time, and explore drivers of the AD by 1) developing a detailed terrestrial stratigraphic framework during the early Permian in the Liujiang Coalfield, North China constrained by our new U-Pb zircon dating from interbedded tuffaceous horizons; 2) identifying major environmental changes during the Artinskian stage, including C cycle perturbations using $\delta^{13}C_{org}$ and weathering by Chemical Index of Alteration (CIA) proxies; 3) obtaining the terrestrial volcanism record and Hg source using Hg anomaly and Hg isotope ratios; and 4) constructing sedimentary records of wildfire through kerogen analysis.

2. Geological setting

During the early Permian, the North China Plate (NCP) was positioned on the northeastern margin of the Paleo-Tethys Ocean at a latitude of approximately 20–30°N (Fig. 1a; Scotese, 2014) with the Inner Mongolia Uplift (IMU) to the north and the Funiu ancient land to the south. The stratigraphic succession, rock types, and marker beds of the strata in the Liujiang Coalfield are shown in Fig. 1c. In this succession, four gray-white claystone beds (named #D, #C, #B, and #A in ascending order; Fig. 1c) are interpreted to have originated as air-fall tuffs (Lu et al., 2021a) that were deposited alongside other clay fractions; we term these lithologies tuffaceous claystones. Each of them contains abundant, well-sorted, euhedral zircon crystals of volcanic origin, which are suitable for U-Pb radiogenic isotope dating. In this area, the sedimentary succession comprises in ascending order the Benxi, Taiyuan, Shanxi, and Lower Shihhotse formations (Shang, 1997; Shao et al., 2020; Wu et al., 2021). We focus on the upper part of the Taiyuan Formation and the Shanxi Formation that collectively comprise dark-gray mudstones with sandstones, thin coal seams and tuffaceous claystone; these were mainly deposited in a delta plain environment (Fig. 1b; Shang, 1997; Shao et al., 2020).

Based on the composition of fossil plant and sporopollen assemblages, the upper parts of the Taiyuan and Shanxi formations have been approximately assigned to the Asselian–Sakmarian and Artinskian–Kungurian stages of the Permian, respectively (Fig. 1c; Wang, 2010). However, in the Paleozoic, fossil plant and sporopollen biostratigraphy in terrestrial settings typically provide comparatively coarse stratigraphic resolution in contrast to more precise methods including U-Pb radiogenic isotope dating. In the Liujiang Coalfield, marked tuffaceous claystone beds #C, #B and #A have not been dated by U-Pb radiogenic isotope dating methods before this study, while marked tuffaceous claystone bed #D (Fig. 1) was dated by Lu et al. (2021a) to 301.2 ± 3.3 Ma. In this paper we provide new U-Pb dates tuffaceous claystone beds #C and #B. Since the lithostratigraphy of North China is diachronous (for detail see Lu et al., 2021c; Zhang et al., 2022), these new zircon ages were used to constrain the stratigraphy in this study area.

3. Materials and analytical methods

Our study is based on two tuffaceous claystone samples, LJC and LJB in ascending order from marked tuffaceous claystone beds #C and #B (Fig. 1), and 30 mudstone samples taken from the ZK-3809 borehole
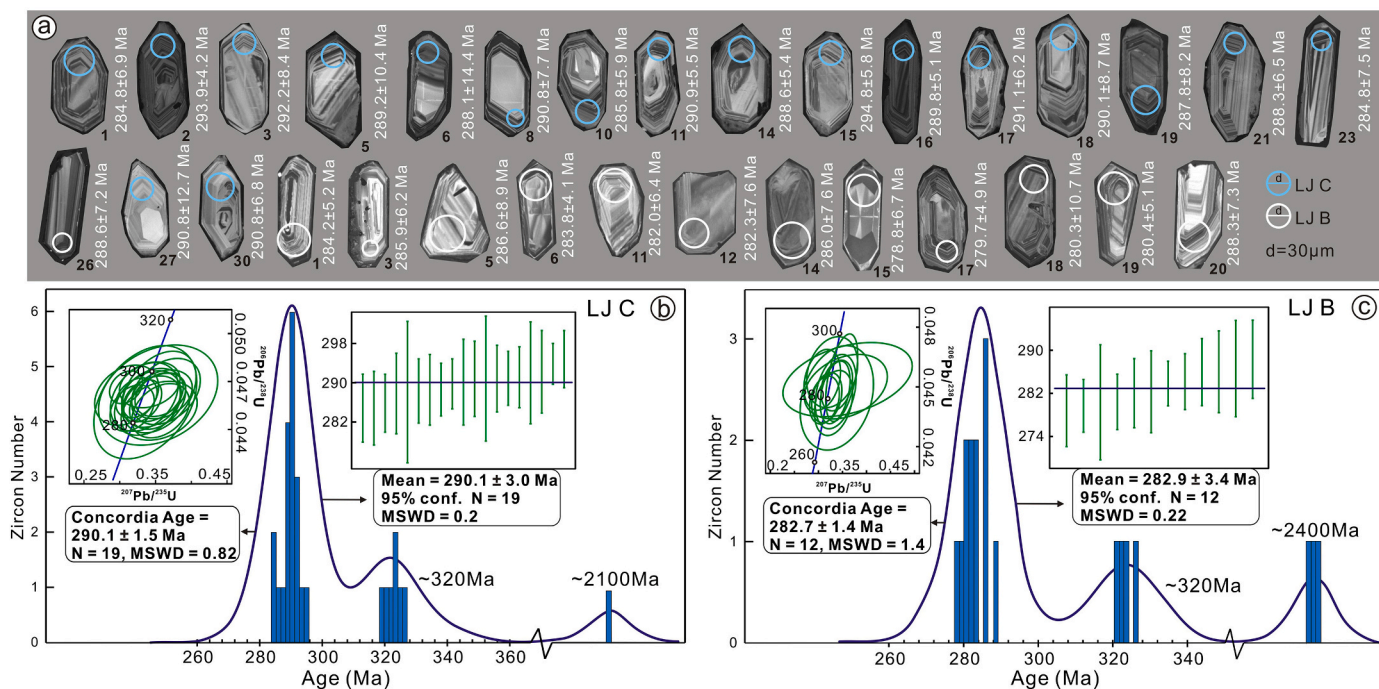
Fig. 2. Zircon ^{206}Pb/^{238}U age distribution diagrams. a, Example zircon crystals from each sample. b, Zircon ^{206}Pb/^{238}U age of sample LJ #C from #C in Fig. 1c. c, Zircon ^{206}Pb/^{238}U age of sample LJ #B from #B in Fig. 1c.

core (40.1005°N, 119.5939°E) that was drilled through the Taiyuan and Shanxi formations in the Liujiang Coalfield.

For U-Pb radiogenic isotope dating of zircon grains from the clay-stones, after crushing, grinding, sieving and heavy liquid and magnetic separation, euhedral zircon crystals that exhibited clear oscillatory zoning under the cathodoluminescence (CL) microscope were selected for U-Pb zircon isotope analysis. U-Pb dating was conducted at the Ore Deposit Geochemistry Microanalysis Laboratory, affiliated to the State Key Laboratory of Geological Processes and Mineral Resources, China University of Geosciences. Laser sampling was performed using a Coherent's GeoLasPro-193 nm system. A Thermo Fisher X-Series 2 ICP–MS instrument was used to acquire ion-signal intensities. Helium was applied as a carrier gas. Argon was used as the make-up gas and mixed with the carrier gas. All data were acquired on zircons in single spot ablation mode at a spot size of 32 μm with 6 Hz frequency in this study. Standard material SRM610 from National Institute of Standards and Technology (NIST) of America was used to optimize the ICP–MS instrument, and as an external standard for determination of trace elements. Zircon 91,500 was used as an external standard for U-Th-Pb isotopic ratios (e.g., Wiedenbeck et al., 2004). Plešovice Zircon was used as a monitoring standard for each analysis (Sláma et al., 2008). Time-dependent drifts of U–Th–Pb isotopic ratios were corrected using a linear interpolation (with time) for every five analyses according to the variations of 91,500 (i.e., 2 zircon 91,500 + 5 samples +2 zircon 91,500). The result of our study shows that the single point analysis of Plešovice zircon and 91,500 is <2.2% (Table S1). Each analysis incorporated a background acquisition of approximately 20s (gas blank) followed by 50s data acquisition from the sample. Off-line selection and integration of background and analyte signals, and time-drift correction and quantitative calibration for trace element analyses and U-Pb dating ages were performed by ICPMSDataCal (Liu et al., 2008) and ages are derived by the LA-ICP-MS method. Age calculations and concordia diagram were carried out using Isoplot 3.0.

For the other analyses, mudstone samples were crushed to <1 mm powder and then divided into two parts. One part was prepared for kerogen enrichment and identification according to the China National Standard (SY/T5125–2014). Kerogen was extracted from the sediment by acid-base treatment using HCL and then HF, followed by liquid flotation to isolate and condense it before being picked up by an eyedropper and transferred onto a microscope slide. On the slide, samples were moved sequentially to give equal spacing, with no <300 effective kerogen macerals (sapropelinite, inertinite, vitrinite and exinite) per slide to be analyzed. Another part was powdered to <200 mesh and divided into six subparts for analysis of (1) mercury concentrations and isotope composition, (2) total organic carbon (TOC) and total sulfur (TS), (3) organic C isotopic composition (δ^{13}C$_{org}$), (4) total nitrogen (TN), (5) major elements (Al$_2$O$_3$, CaO, P$_2$O$_5$, Na$_2$O and K$_2$O), and (6) trace elements (Th and U).

Mercury concentrations were measured at the State Key Laboratory of Coal Resources and Safe Mining (Beijing) with a mercury analyzer (Lumex RA-915+) with lower detection limits of 2 ng/g (2 ppb) and relative analytical error of ±5%. A subset of samples (*n* = 15) was analyzed for Hg isotopes at Tianjin University and Hg isotopic results are expressed as δ^{***}Hg (‰, *** = 199, 200, 201, 202, 204) relative to the bracketed NIST 3133 Hg standard, and MIF value is denoted as Δ^{xxx}Hg (‰, xxx = 199, 201), representing the difference between the measured δ^{***}Hg value and that predicted from δ^{202}Hg using a kinetic MDF law (for more details see (Sun et al., 2020)). Except for the Hg geochemistry, other geochemical analyses were undertaken at Beijing Research Institute of Uranium Geology, and the detailed descriptions of analytical methods and errors used followed those of (Lu et al., 2021a, 2021b, 2021c).

Chemical Index of Alteration (CIA) was used to indicate the weathering trends of the source area. High CIA values (>85) reflect relatively strong weathering in warm-humid climates, the CIA values between 65 and 85 reflect moderate weathering, while low CIA values (<65) reflect relatively weak weathering (Fedo et al., 1995). The concept, application and calculation of CIA followed standard protocols (Nesbitt and Young, 1984; Roy and Roser, 2013). Values of CaO* (CaO* = CaO in the silicate fraction only) were calculated by the indirect calculation method of (McLennan, 1993), and the influence of K metasomatism throughout the diagenetic stage (time interval from the burial of sediments to the time before metamorphism) was corrected by the triangular chart of A-CN-K [Al$_2$O$_3$-(CaO* + Na$_2$O)-K$_2$O] proposed by (Nesbitt and Young, 1984).
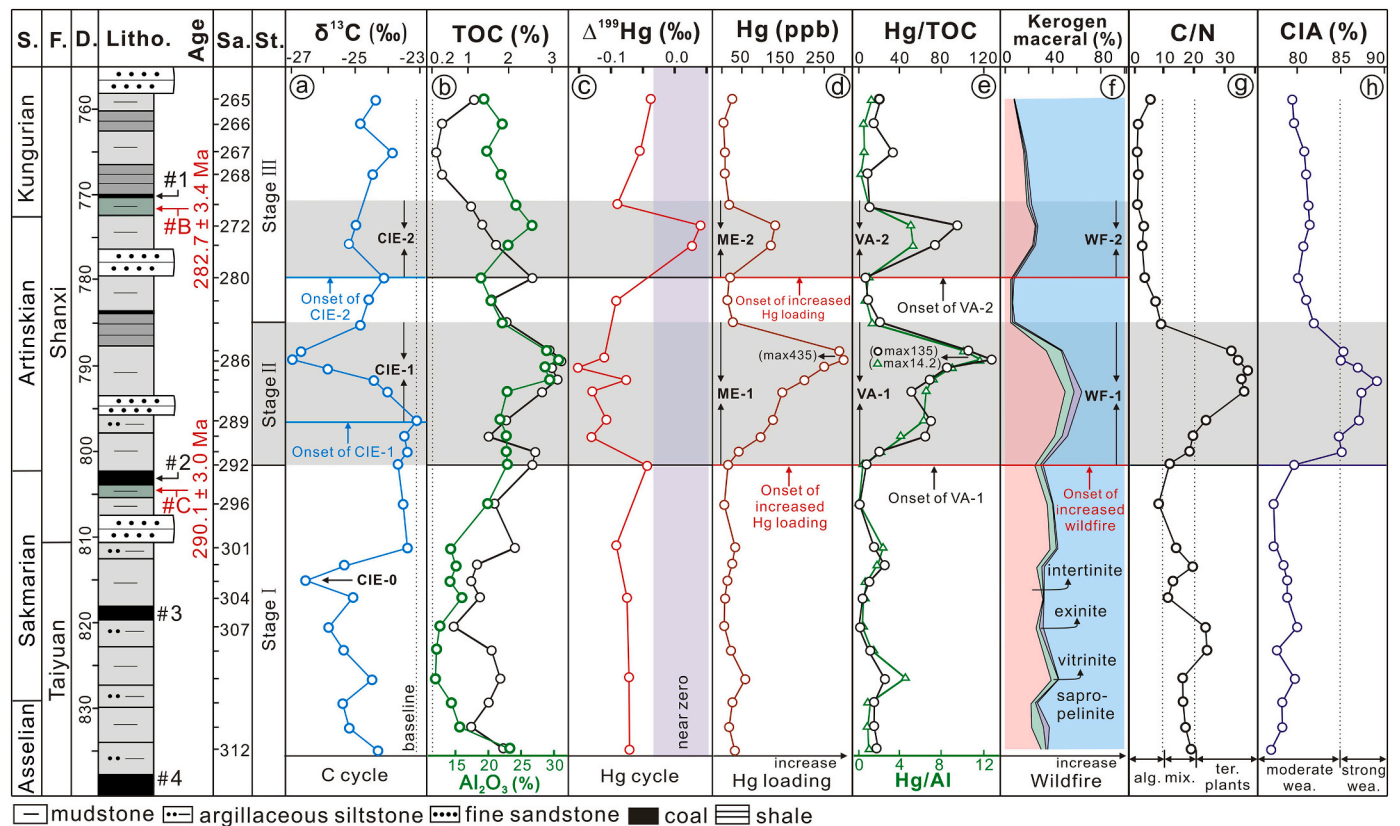
Fig. 3. Results of organic carbon isotope composition (δ13Corg, ‰), total organic carbon (TOC) contents (%), Δ199Hg, Hg contents (ppb), Hg/TOC ratios (ppb/%), Hg/Al ratios (ppb/%), Kerogen maceral (%), C/N ratios, and CIA values from the ZK-3809 drillhole in the Lujiang Coalfield. Abbreviations: S. - Stage; F. - Formation; D. - depth; Litho. - lithofacies; M. – marker bed; Sa. - sample; Kun. – Kungurian; Asse. – Asselian.

4. Results and analysis

4.1. U-Pb zircon dating

More than 1600 and 1300 zircon crystals were separated from samples #LJC and #LJB, respectively, in the ZK-3809 borehole from the Liujiang coalfield, with crystal sizes varying from 50 to 200 μm in maximum length. Most crystals show euhedral morphology and clear oscillatory zoning in cathodoluminescence, (CL) distinctive of zircons with a magmatic origin (Fig. 2a). The zircon Th/U ratios vary from 0.16 to 1.15 (arithmetic mean (x̄) = 0.66, Table S1) also indicate their volcanic origin.

$^{206}Pb/^{238}U$ dating results for samples #LJC and #LJB are shown in Fig. 2 and Table S1. From sample #LJC, 27 concordant age values were determined with three distribution peaks (Fig. 2b); the younger peak has a concordia age of 290.1 ± 1.5 Ma (MSWD = 0.82, and N = 19, uncertainties are given at the 2σ level, the single-point analytical error of standard zircon Plešovice and 91,500 is <2.2%) and the weighted mean $^{206}Pb/^{238}U$ age of 290.1 ± 3.0 Ma (MSWD = 0.2, N = 19). Sample #LJB yielded 19 concordant age values with three distribution peaks (Fig. 2c), the youngest peak has a concordia age of 282.7 ± 1.4 Ma (MSWD = 1.4, N = 12) and a weighted mean $^{206}Pb/^{238}U$ age of 282.9 ± 3.4 Ma (MSWD = 0.22, N = 12) (Fig. 2). We interpret the ages from the youngest peaks as the sedimentary ages of the tuffaceous claystone horizons (e.g., Lu et al., 2021a).

Based on the two new zircon ages from sample #LJC and #LJB, using linear interpolation and without applying differential compaction correction or considering different rates of deposition, the studied strata from the upper part of Taiyuan to the Shanxi formations was constrained stratigraphically to the late Asselian to early Kungurian (Fig. 3). This age is consistent with the Cisuralian age inferred by biostratigraphic

syntheses (Wang, 2010).

4.2. Elemental geochemistry

Results of major and trace elements and calculated carbon to nitrogen (C/N) ratios are shown in Fig. 3 and Table S2. Total organic carbon (TOC) values vary from 0.26% to 3.20% (x̄ = 1.74%) and show an increasing trend from 1.03% to 3.20% during the latest Asselian to the early Artinskian followed by a decreasing trend from 3.20% to 0.5% from the late Artinskian to the early Kungurian (Fig. 3b; Table S2).

C/N ratios vary from 1.51 to 37.50 (x̄ = 15.86), and vertically show a gradual decreasing trend from 20 to 10 (x̄ = 17.26) in the late Asselian–Sakmarian (Stage I), a peak stage (x̄ = 27.40) with high values in the early Artinskian (Stage II), and a stable stage with low values (x̄ = 3.92) in the late Artinskian–early Kungurian (Stage III) (Fig. 3g; Table S2). C/N ratios have been used to evaluate the organic matter (OM) source of sediments. High (C/N ratios >20) indicate OM originates from terrestrial plants, while low C/N ratios (<10) indicate OM originated from algae in the lake, with moderate values indicating a mixed source of sedimentary OM (Meyers and Lee, 1994). Consequently, Stage I represents a period of OM mixing from terrestrial and lake sources, Stage II OM originates from terrestrial plants, and Stage III OM is from algae in the lake.

4.3. Chemical weathering records

Chemical Index of Alteration (CIA) was used to indicate the weathering trends of the source area. The concept, application and calculation formula of CIA followed standard protocols (Bhatia and Taylor, 1981; Nesbitt and Young, 1984; Roy and Roser, 2013). Chemical index of alteration (CIA) values calculated from major element data are shown in
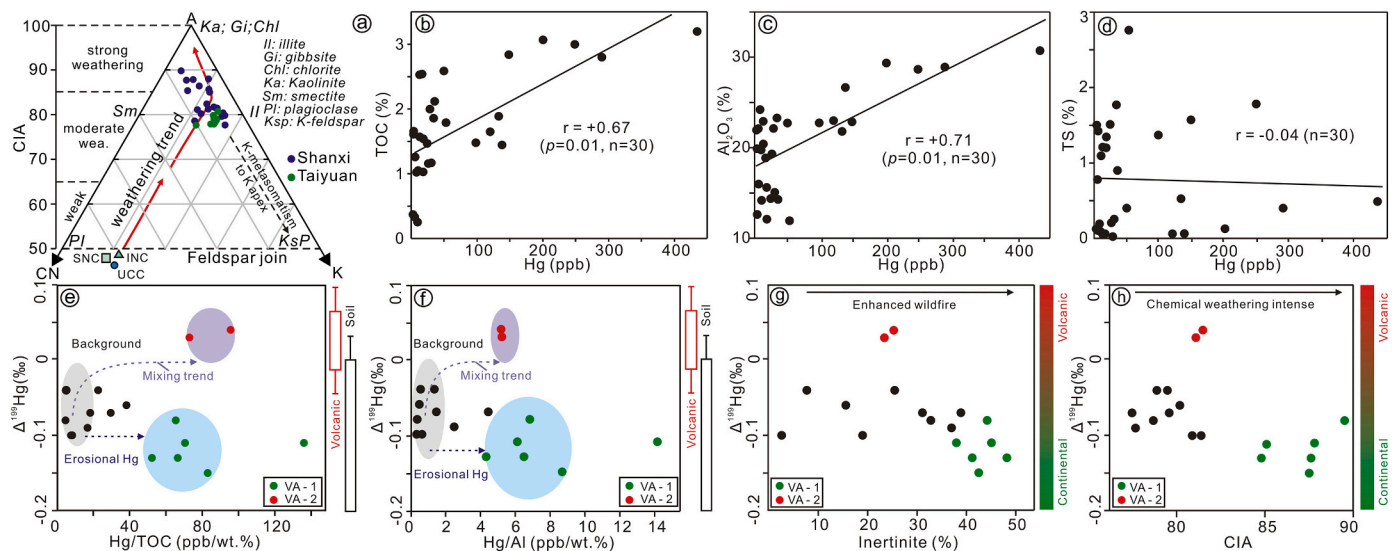
Fig. 4. Crossplots of: Hg and TOC; Hg and Al; and Hg and TS. "r" represents the positive (+) correlation coefficient, "n" represents the number of samples. d, A-CN-K diagram of mudstone samples from Taiyuan and Shanxi with the chemical index of alteration (CIA) scale to the left. e-h, Hg source analysis, base map from Shen et al. (2022a). For comparison, the average upper crust CIA value of southern and interior North China Craton are shown (modified from Cao et al., 2019). Also plotted are the molar proportions of southern North China upper crust (SNC), interior North China upper crust (INC), and average upper continental crust (UCC). Abbreviations: A = Al$_2$O$_3$; CN = CaO* + Na$_2$O; K = K$_2$O; CIA = chemical index of alteration.
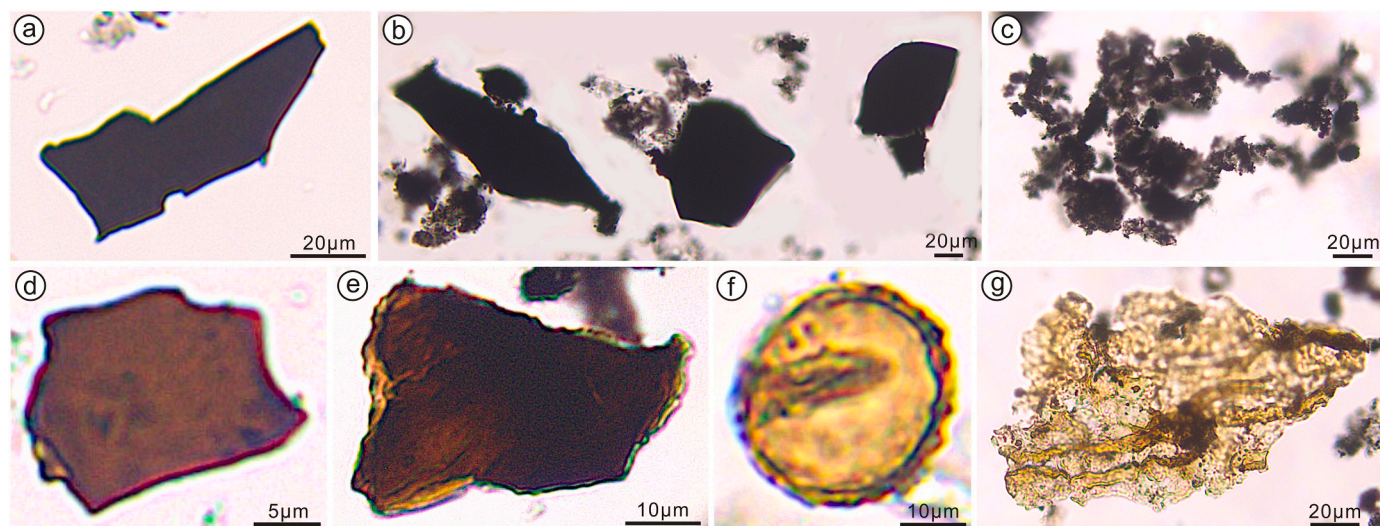

Fig. 5. Photomicrographs showing microstructural characteristics of kerogen macerals in the study area: a-b, fusinite (transmitted light, sample LJ286 and LJ288); c, sapropelinite (transmitted light, sample LJ265); d-e, collinite (transmitted light, sample LJ265 and LJ282); f, sporinite (transmitted light, sample LJ301). g, suberinite (transmitted light, sample LJ290).

Table S2. Using Th/U ratios (c.f. Bhatia and Taylor, 1981) and the Al$_2$O$_3$-CaO* + Na$_2$O-K$_2$O (A-CN-K) diagram (Nesbitt and Young, 1984), the effect of sedimentary recycling and potassium metasomatism alteration on CIA was evaluated. Th/U ratios vary from 3.47 to 5.43 (Table S2), indicating that the parent rocks of the sediments in the study area are not recycled. This agrees with Shang (1997) who determined sediments of the study area mainly originated from the Inner Mongolia Uplift. In the A-CN-K diagram (Fig. 4a) the distribution trend of samples with CIA values <85 is approximately parallel to the A-CN boundary, while the distribution of samples with high CIA values (CIA >85) is subparallel to the A-K boundary, but trends to the vertex A gradually, indicating that the samples of the study area are less affected by potassium metasomatism alteration in the diagenetic stage (Nesbitt and Young, 1984). As a result, in this study CIA values are a robust proxy reflecting the weathering trends of the source area.

As shown in Fig. 3, CIA values vary from 77.5% to 89.5% ($\bar{x}$ = 81.5%; Fig. 3h), indicating moderate to strong weathering conditions of the source area. Vertically through the succession, stable and moderate weathering conditions prevailed during the late Asselian to Sakmarian and the late Artinskian to early Kungurian stage respectively ($\bar{x}$ =78.5 and 80.5 respectively; Fig. 3h), but a period of strong weathering occurred during the early Artinskian with CIA values from 82.1 to 89.5 ($\bar{x}$ =86.2; Fig. 3h).

4.4. Kerogen macerals and records of wildfire

As shown in Fig. 3 and Table S2, kerogen macerals in the study mainly comprise sapropelinite and inertinite, followed by vitrinite and exinite. Sapropelinite content varies between 36.4 and 95.6% of the maceral content ($\bar{x}$ = 65.5%; Fig. 3f and Fig. 5c). Vitrinite content
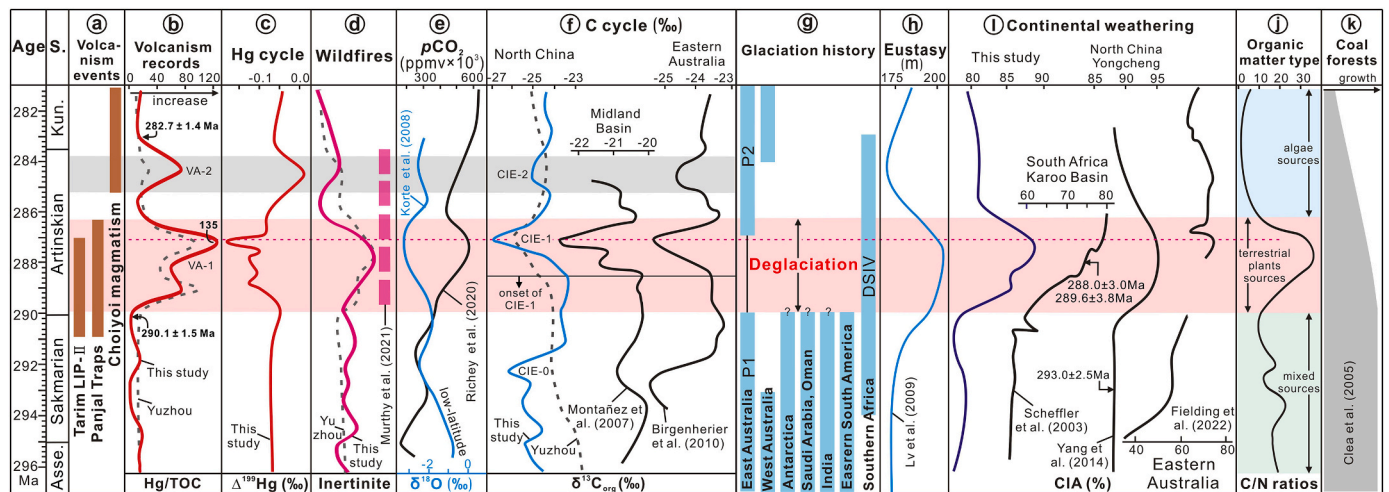
Fig. 6. Correlation of Sakmarian –Artinskian boundary global events. a, Volcanic activity curve of study area and timing of the Tarim II LIP, Panjal Traps, Qiangtang intrusions and Choiyoi magmatism (Xu et al., 2014; Shellnutt, 2018; Zhang and Zhang, 2017; Sato et al., 2015 and reference therein). b-c, volcanism recorded, Hg cycle and wildfire in the study area. d, Global pCO_2 concentration from (Richey et al., 2020), and $\delta^{18}O$ from (Korte et al., 2008). f, $\delta^{13}C$ variation (Montañez et al., 2007; Birgenheier et al., 2010) compared to that of Liujiang Coalfield (ZK-3809). g, glaciation history from Fielding et al., 2023 and references therein, Montañez and Poulsen, 2013 and references therein. h, eustasy change from (Ross and Ross, 1987). i, CIA trend (Scheffler et al., 2003; Yang et al., 2014; Fielding et al., 2023) compared to that of Liujiang Coalfield. j, OM types in the study area. k, aerial extent of coal forests from (Cleal et al., 2005).

varies from 0.5 to 11.2% ($x^- = 4.6\%$) and comprises non-fluorescent telinite and collinite (Fig. 3f and Fig. 5d, e). The exinite group, with contents varying from 0 to 7.4% ($x^- = 2.8\%$) and mainly comprises sporopollenite and suberinite (Fig. 3f and Fig. 5f, g). Inertinite content varies from 2.4 to 48.2% ($x^- = 27.1\%$; Fig. 3f) of the maceral content and has an obvious peak abundance during the early Artinskian and remains high during the mid-Artinskian. Inertinite content is entirely composed of fusinite (charcoal) which is opaque, pure black, and does not fluoresce under fluorescence illumination and is mostly long and thin or fragmental in shape with sharp edges (Fig. 5a–b), indicating that it has not undergone significant transport that would break it into smaller pieces.

Fusinite is the product of incomplete combustion (Guo and Bustin, 1998; Bustin and Guo, 1999), and inertinite debris is common in peat following wildfires (Goodarzi, 1985; Glasspool and Scott, 2010; Scott, 2010). The provenance of the study area is the Inner Mongolia Uplift to the north, which consists of eroded rocks of Precambrian age (Shang, 1997). Given that there were no terrestrial plants during the Precambrian (e.g., Taylor et al., 2009), and that the earliest stratigraphical occurrence of charcoal in the geological record is from the Silurian period (Glasspool et al., 2004), inertinite in the study area could not have been reworked and transported from the provenance lithologies. U/Th values vary from 0.18 to 0.29 (Table S2), and values <0.75 (Jones and Manning, 1994; Pattan et al., 2005) are considered to indicate that the same degree of oxidation is present through the vertical succession. The U/Th values exclude the influence of sedimentary environment and diagenesis on variations in inertinite content. Thus, we consider the fusinite in our samples to be a reliable proxy for wildfire during the time of deposition. The inertinite content in our study records two peaks that we interpret as two intervals of enhanced wildfire (WF-1 and WF-2) during the early and late Artinskian respectively.

4.5. Hg geochemistry

Results for Hg contents and isotope ratios are shown in Fig. 3c, d and Table S2, S3. Mercury contents vary from 3 ppb–435 ppb ($x^- = 74.1$ ppb) (Fig. 3c) and show a major mercury enrichment (ME) peak during the early Artinskian (ME-1) followed by a minor peak during the latest Artinskian (ME-2). The two peaks are synchronous with CIE-1 and CIE-2 negative $\delta^{13}C_{org}$ excursions, respectively, but the onset of ME-1 is earlier

than the onset of CIE-1. Mercury contents show stronger covariations with TOC (correlation coefficient (r) = +0.67 with 99% confidence level; $n = 30$) and Al (r = +0.71 with 99% confidence level, n = 30) than with total sulfide (TS; $r = -0.04$; n = 30) (Fig. 4b–d), suggesting Hg is mostly hosted by organic matter and clay fractions. Therefore, we present the values of Hg/TOC and Hg/Al to evaluate Hg concentration enrichments. Values of Hg/TOC vary from 2.05 to 135.94 ppb/wt% ($x^- = 35.00$ ppb/wt%), Hg/Al vary from 0.14 to 14.16 ppb/wt% ($x^- = 3.06$ ppb/wt%), and both show a pattern similar to Hg concentrations. The two peaks in Hg/TOC and Hg/Al (VA-1 and VA-2) coincide with the positions of CIE-1 and CIE-2 respectively, and the onset of VA-1 slightly predates the onset of CIE-2. We surmise that VA-1 and VA-2 represent sedimentary records of volcanic activity and its ripple effects (wildfires, terrestrial runoff) during the early and latest Artinskian, respectively (e. g., Lu et al., 2021b, 2021c). As shown in Fig. 2, values of odd Hg isotope MIF ($\Delta^{199}Hg$) vary from $-0.15\permil$ to $0.04\permil$ ($x^- = -0.08\permil$; $n = 17$). During VA-1, $\Delta^{199}Hg$ show a small but systematic negative excursion of $-0.15\permil$ from zero ($\Delta^{199}Hg$ of volcanic-sourced Hg), but near zero (0.03‰, 0.04‰) during VA-2. $\Delta^{199}Hg$ values show a stable trend during the late Asselian–earliest Artinskian and late Artinskian–early Kunguian, respectively, corresponding to the observed low Hg content intervals. The onset of the interval of strong weathering is synchronous with the start of volcanic activity VA-1 and increased Hg loading, but slightly predates the onset of the negative excursion of CIE-1.

4.6. $\delta^{13}C_{org}$ chemostratigraphy

Results of $\delta^{13}C_{org}$ are shown in Fig. 3 and Table S2 and provide a stratigraphic framework for chemostratigraphic correlation with comparable records from other regions. $\delta^{13}C_{org}$ values vary from $-23.1\permil$ to $-27.0\permil$, with an average of $-24.7\permil$ (Fig. 3a). These show a gradual negative excursion from the late Asselian–middle Sakmarian from $-26.6\permil$ to $-24.2\permil$ with a magnitude of 2.4‰ (CIE-0), a positive carbon isotopic excursion from the late Sakmarian–earliest Artinskian ($x^- = -23.5\permil$), and negative excursions in the early Artinskian with a magnitude of 3.9‰ (CIE-1) and latest Artinskian with a smaller magnitude of 1.9‰ (CIE-2) (Fig. 3a).
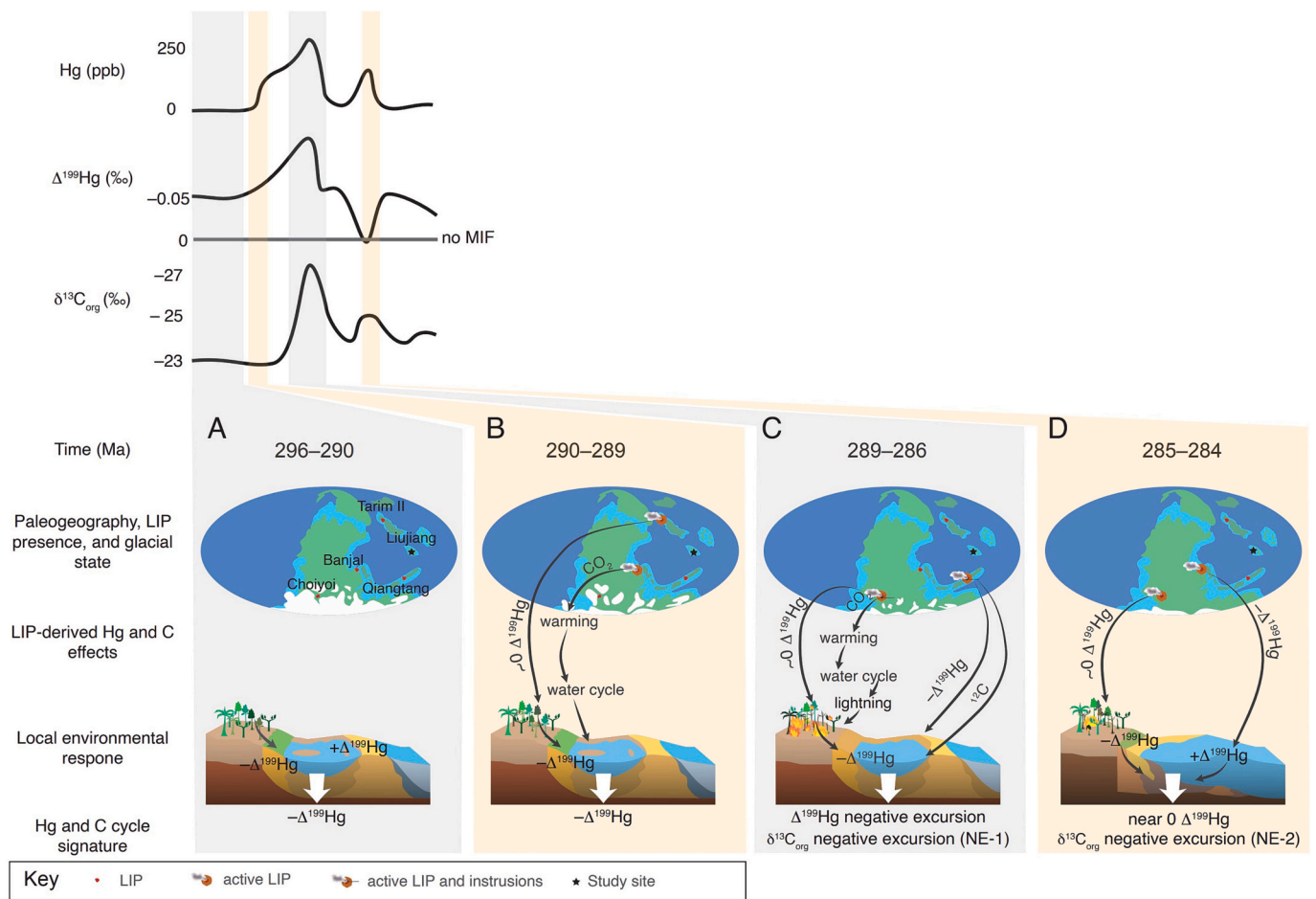
Fig. 7. Reconstructions of glacial to interglacial continental ecological phases with schematic diagram illustrating conceptual Hg flux from late Sakmarian to Artinskian time, a shows normal condition in the main glacial. b shows the onset of Hg inputs and wildfire, Tarim II LIP and Panjal Traps eruption period at the onset of deglaciation. c shows the additional preferential Hg loading in terrestrial environments related to plant combustion and soil erosion sources during the maximum of Artinskian deglaciation. d shows environmental change during the interglacial.

5. Discussion

5.1. Environmental changes during the Artinskian

In the study area, the Artinskian deglaciation (AD) is linked by a synchronous negative C isotope excursion, Hg cycle anomaly, increased continental weathering and rising sea level (Ross and Ross, 1987) (Fig. 6). The $\delta^{13}C_{org}$ curve shows three negative excursions in the studied interval, during the late Asselian–middle Sakmarian with an offset of 2.4‰ (CIE-0), in the early Artinskian with the largest excursion of 3.9‰ (CIE-1), and in the latest Artinskian with the smallest excursion of 1.9‰ (CIE-2) (Fig. 3a). Elsewhere, a bimodal $\delta^{13}C_{carb}$ negative excursion is observed around the Asselian–Sakmarian boundary and has been suggested as a potential chemostratigraphic marker for the Asselian-Sakmarian stage boundary (Zeng et al., 2012). $\delta^{13}C_{org}$ values in the study area show a negative excursion at the Asselian–Sakmarian boundary, and show another negative excursion during the mid-Sakmarian (CIE-0, 2.4‰ excursion).

In the study area $\delta^{13}C_{org}$ values increase first and then decrease during the early Artinskian (CIE-1), with a negative excursion of about 3.9‰. A similar chemostratigraphic pattern occurs in the Midland Basin in the Urals (Fig. 6f; Montañez et al., 2007), East Australia (Fig. 6f; Birgenheier et al., 2010), the Yuzhou and Huainan coalfields (North China Platform, Zhang et al., 1999; Lu et al., 2021c), the Xikou section (Central China, Cheng et al., 2019), the Rockland section and the Orogrande Basin (USA, Tierney, 2010; Koch and Frank, 2012). A good

correlation exists between $\delta^{13}C_{org}$ and $\delta^{13}C_{carb}$ records, so the $\delta^{13}C_{org}$ pattern in the Artinskian may represent a global trend (Lu et al., 2021c) which is isochronous with the AD. In the study area, $\delta^{13}C_{org}$ shows a negative excursion in the late Artinskian (CIE-2, 1.9‰ offset) that correlates with a similar CIE in the Midland Basin in the Urals (Fig. 6f; Montañez et al., 2007), and East Australia (Fig. 6f; Birgenheier et al., 2010). However, so far this feature has not been noted elsewhere.

Enhanced continental weathering during the AD is isochronous with CIE-1, reflected by increased CIA values in the study area. Our CIA values show enhanced weathering ocurred during the early Artinskian. Enhanced weathering also occurred in early Artinskian sedimentary sequences in the Yongcheng Basin (North China, Yang et al., 2014), and in Gondwana from the Satpura Basin (India, Roy and Roser, 2013), the Karoo Basin (South Africa, Scheffler et al., 2003), the Paraná Basin (South America, Goldberg and Humayun, 2010) (Fig. 6j), and based on CIA results also in eastern Australia (Fielding et al., 2023). Results from strontium and lithium isotopes also confirm enhanced global continental weathering during early Artinskian (Cao et al., 2022 and references therein). Thus, increased continental weathering during the Artinskian appears to be a global signal. However, CIE-2 is not as distinct as CIE-0 and CIE-1 and is based on values from two samples, but coincides with anomalous Hg levels; higher resolution $\delta^{13}C_{org}$ sampling frequency is needed to confirm the exact position and magnitude of CIE-2.

In addition to the global $\delta^{13}C_{org}$ excursion and global continental weathering trends, in the study area the AD was also accompanied by environmental changes that inlude changing OM types from mixed

sources to terrestrial plant dominated, collectively indicating rising sea level (Ross and Ross, 1987). Previous sequence stratigraphic studies across the North China Plate identified sea level rise at this time (Fig. 6i, Lv et al., 2009). Marine successions in the Sydney Basin evidence a 30 m sea level rise as demonstrated by facies juxtapositions (Fielding et al., 2008), suggesting this is a global transgression and a marker for the AD.

5.2. Contributors of C and Hg cycles during the Artinskian

In the study area, sedimentary mecury enrichment peaks VA-1 and VA-2 are synchronous with CIE-1 and CIE-2 respectively, indicating the co-sources of mercury and carbon from magmatic heating of organic-rich sediments (Vervoort et al., 2019; Shen et al., 2020a). The available candidates for Artinskian volcanism include the Tarim-II LIP, the Panjal traps, and Choiyoi volcanism (Xu et al., 2014; Sato et al., 2015; Shellnutt, 2018; Fielding et al., 2023). Existing data show that volcanism of the Tarim-II LIP, Panjal traps, and Choiyoi volcanism are mainly characterized by intermediate acid rocks including rhyolite, dacite, andesite and pyroclastics (Xu et al., 2014, Sato et al., 2015 and reference therein; Shellnutt, 2018). This type of volcanism can release lage amounts of Hg and C into the atmosphere and can cause increased environmental Hg loading (e.g., Lu et al., 2021c), as recorded in the study area. The Tarim-II LIP and Panjal traps have good stratigraphic correspondance with the negative carbon isotope excursion CIE-1 and Hg flux peak VA-1, and Choiyoi volcanism has good stratigraphic correspondance with negative carbon isotope excursion CIE-2 and Hg flux peak VA-2. However, none of the published stratigraphic ages for these volcanic events correlate with CIE-0 (Fig. 6). We consider the onset of CIE-1 to mark commencement of volcanism of the Tarim-II LIP and Panjal traps, while the onset of CIE-2 marks the commencment of Choiyoi volcanism (Figs. 6, 7). We consider that CIE-0 is not caused by volcanism but its causes need further study to elucidate.

A multi-end member mixing model of Hg can evaluate sources of mecury enrichment during ME-1, ME-2 and the remaining intervals (e. g., Shen et al., 2022a). Before VA-1, Δ^{199}Hg shows negative values, and lower Hg/TOC and Hg/Al values indicate background levels from terrestrial sources, as seen in sediments from other locations and stratigraphic intervals dominated by terrestrial Hg sources (Yin et al., 2016; Shen et al., 2020a). During VA-1, Δ^{199}Hg, Hg/TOC and Hg/Al covariation suggest terrestrial Hg sources (blue ellipse in Fig. 4e, f) characterized by higher Hg/TOC, Hg/Al and more negative Δ^{199}Hg, with values similar to those from the background interval. During VA-2, Δ^{199}Hg, Hg/TOC and Hg/Al covariations suggest atmospherically transported volcanic Hg (purple ellipse in Fig. 4e, f) characterized by higher Hg/TOC, Hg/Al and near-zero or slightly positive Δ^{199}Hg values; this may come directly from the atmosphere or from the water column

(Shen et al., 2022a). Except for the VA-1 and VA-2 intervals, the covariation shows the mixing trends with background Hg as one end member (gray ellipse in Fig. 4e, f).

The relatively strong correlations (r = +0.67; r = +0.71) between Hg, TOC and Al suggest that in addition to direct atmospheric deposition, terrestrial input is another major Hg source in the study area, and the higher Hg-Al relationship is a by-product of TOC-Al covariation (r = +0.93). This is likely because of the shallow-water and offshore depositional setting of the strata (Fig. 7; Shao et al., 2020). During VA-1, the systematic negative Δ^{199}Hg shift indicates that large amounts of Hg-enriched OM (with negative MIF values) were transported into the basin and cover the near-zero MIF signal from direct volcanic gas deposition (Blum et al., 2014). At the same time, this is supported by the co-increase in C/N ratios (>20) and the content of terrigenous maceral (including intertinite, vitinite and exinite) in kerogen (>50%). However, during VA-2, C/N ratios decreased to <10, indicating a main OM source of hydroplanktonic algae, which is consistent with the higher sapropel kerogen maceral content (~80%). Together with the near-zero MIF value, these all suggest the primary Hg source was either direct volcanic gas deposition (Fig. 7), or equal mixing of atmospheric (positive MIF) and terrestrial (negative MIF) Hg sources (Shen et al., 2022b).

5.3. Volcanism and wildfires as co-drivers for the Artinskian Deglaciation

Wildfire is an important trigger mechanism for releasing stored terrestrial C and Hg as seen in the study area by the coincident rise of inertinite content as direct evidence of wildfire (WF-1 and WF-2) and changes in C and Hg isotopes (Fig. 3f). WF-1 also has a good correlation with the biggset $\delta^{13}C_{org}$ excursion (CIE-1) and enhanced global continental weathering, WF-2 has a good correlation with the $\delta^{13}C_{org}$ excursion (CIE-2). Recent studies have shown that wildfires were frequent in the Rajmahal Basin (India) and the Yuzhou Basin (southern North China) during the Artinskian (Murthy et al., 2021; Lu et al., 2021c); increased incidence of wildfire during the Artinskian may be a global signaal. In the study area, WF-1 is much bigger than WF-2, soil erosion was stronger, and continental weathering was more significant than in the VA-1 interval. Therefore, even if there were a large number of near zero Δ^{199}Hg signals from the direct release of a volcanism during the VA-1 interval, these were also overprinted by terrestrial Hg signals transported by huge soil erosion.

An alternative explanation for the co-occurrence of the negative carbon isotope excursions with Hg flux peaks is the environmental and climatic effects caused by volcanism. In the study area, the onset of the two wildfires were synchronous with the beginning of increased Hg loading (VA-1 and VA-2); synchronization of the peaks in indices for wildfire, Hg flux, and negative CIEs suggest that volcanism is responsible

(1) Intensified hydrological cycle produces lightning, ignite wildfire   (3) Increased oxidation of OM in the biosphere
(2) Increased oxidation of soil OM in the pedosphere   (4) Increased oxidation of CH_4 in the atmosphere
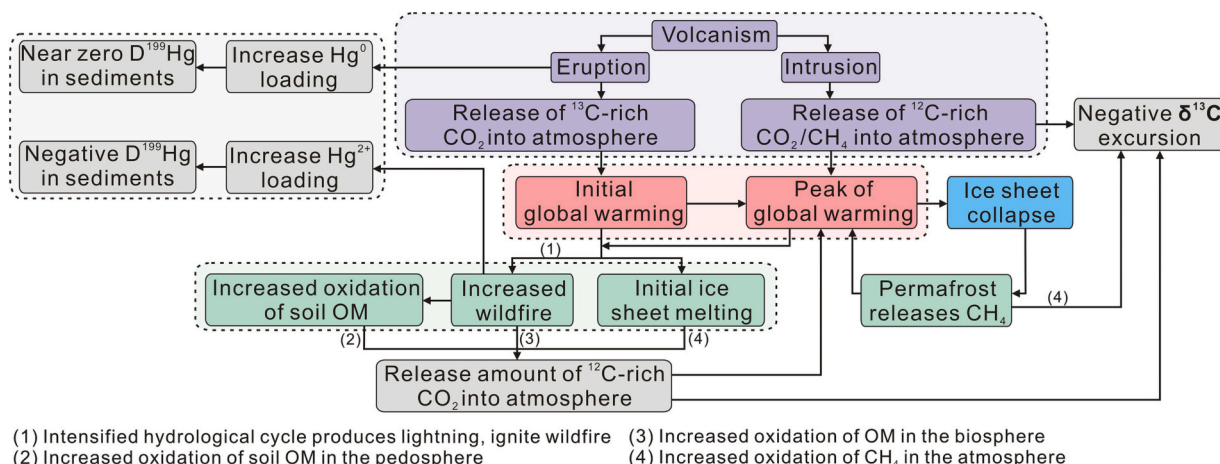
Fig. 8. Coupling relationship between volcanism and environmental changes.

for the increase in Artinskian global wildfire, and that soil erosion caused by wildfire was another important source of Hg (with negative Δ^{199}Hg values). Wildfire also can oxidize organic matter and release C (^{12}C-rich) into the atmosphere (Vervoort et al., 2019; Lu et al., 2022) (Fig. 7). This may have been particularly pronounced during the early Artinskian, when the soil erosion was accompanied by evidence for terrestrial ecosystem collapse indicated by a plant extinction event during the earlist Artinskian, and usually with massive wildfires and a massive influx of Hg (Lu et al., 2021b; Wu et al., 2021; Dal Corso et al., 2022; Shen et al., 2023). Similar findings are also observed during the P–T transition, when modeling of biogeochemical coupling of the global C and Hg cycles indicates that a large Hg peak and nadirs in δ^{13}C are best explained by a sudden, massive pulse of terrestrial biomass oxidation caused by terrestrial ecosystems collapse (Burgess and Bowring, 2015; Burgess et al., 2017; Dal Corso et al., 2022; Shen et al., 2023).

We observe increased charcoal abundance coupled with increasing CIA during CIE-1, indicating a correlation between wildfires and enhanced chemical weathering (Fig. 3). Generally, wildfires are more frequent in arid climates, however, enhanced chemical weathering is more likely to indicate humid and warmer climates. We suggest that perhaps the primary driver of the enhanced chemical weathering we observe is warmer temperatures rather than increased humidity. Another possibility is that the climate was temporally heterogeneous (alternating humid vs dry conditions) which our records are too coarse to resolve. The prevalence of wildfire during the AD may also have been controlled by ignition factors. Under natural conditions, ignition is caused by lightning, volcanic eruption and less probably meteor impact (Jones and Lim, 2000; Glasspool et al., 2015). Of these, during the Artinskian there was no volcanic activity in proximity to the study area suitable to ignite wildfires, nor is there any evidence for meteor impact. Lightning would have been the main ignition source of wildfire, with lightning occurring more frequently in humid climates (e.g., Glasspool and Scott, 2010; Glasspool et al., 2015). In addition, C and Hg trapped in permafrost under the largest LPIA ice sheet released during the deglaciation would also become potential contributors to the co-occurrence of CIE-1 and VA-1 via the added release of C and Hg. More evidence, including the sources of Hg, is needed to further evaluate this possibility.

Coupling relationships between volcanism–climate–wildfire persisted throughout the Artinskian (Fig. 6–8). The co-occurrence of peaks in volcanism and wildfire at the mid-Artinskian coincided with deglaciation during the LPIA, is associated with Hg cycle anomalies, and is earlier than the large negative carbon isotope excursions (Fig. 6). The AD was directly recorded by glacial sediments in Australia (Fielding et al., 2008) and confirmed by brachiopod-based ^{87}Sr/^{86}Sr data in the southern hemisphere (Garbelli et al., 2019). AD is also supported by the transgression from mixed to terrestrial sources in OM types in the study area, and by the contemporary peak in global continental weathering and atmospheric temperature and CO_2 concentrations (Korte et al., 2005; Montañez et al., 2007; Richey et al., 2020). The AD demonstrates a series of cascading Earth system changes (Fig. 8). Volcanism released greenhouse gases and Hg, leading to observed anomalies in both the C and Hg cycles as well as global warming (manifest in enhanced continental weathering). In addition, the terrestrial ecosystems were perturbed, manifest in massive wildfire and enhanced soil erosion, leading to further releases of terrestrial carbon and soil-bound Hg, exacerbating observed C and Hg anomalies. We infer that this series of cascading Earth system perturbations likely ultimately drove the observed ice sheet melting and deglaciation. As our data are based on results from a single borehole, further data are needed to test this hypothesis.

6. Conclusions

Hg concentration and isotope data through a sedimentary core in the northeastern margin of North China show two significant volcanic events occurred during the Artinskian which coincide with the timing of the Tarim-II, Panjal and Choiyoi volcanic provinces. Our study shows

that hypothesized volcanism and wildfires released greenhouse gases, led to ice sheet melting, the release of terrestrial C and resulting C cycle anomalies, and enhanced continental weathering, while wildfires released terrestrial Hg into basin.

Declaration of Competing Interest

The authors declare that they have no competing interests.

Data availability

All data used in the paper is included in the paper or as part of the supplementary files

Appendix A. Supplementary data

Supplementary data to this article can be found online at https://doi.org/10.1016/j.gloplacha.2023.104126.

References

Bhatia, M.R., Taylor, S.R., 1981. Trace-element geochemistry and sedimentary provinces: a study from the Tasman Geosyncline, Australia. Chem. Geol. 33, 115–125.

Birgenheier, L.P., Frank, T.D., Fielding, C.R., Rygel, M.C., 2010. Coupled carbon isotopic and sedimentological records from the Permian system of eastern Australia reveal the response of atmospheric carbon dioxide to glacial growth and decay during the late Palaeozoic Ice Age. Palaeogeogr. Palaeoclimatol. Palaeoecol. 286, 178–193.

Blum, J.D., Sherman, L.S., Johnson, M.W., 2014. Mercury isotopes in earth and environmental sciences. Annu. Rev. Earth Planet. Sci. 42, 249–269.

Burgess, S.D., Bowring, S.A., 2015. High-precision geochronology confirms voluminous magmatism before, during, and after Earth's most severe extinction. Sci. Adv. 1.

Burgess, S.D., Muirhead, J.D., Bowring, S.A., 2017. Initial pulse of Siberian Traps sills as the trigger of the end-Permian mass extinction. Nat. Commun. 8, 164.

Bustin, R.M., Guo, Y., 1999. Abrupt changes (jumps) in reflectance values and chemical compositions of artificial charcoals and inertinite in coals. Int. J. Coal Geol. 38, 237–260.

Cao, C., Bataille, C.P., Song, H., Saltzman, M.R., Tierney Cramer, K., Wu, H., Korte, C., Zhang, Z., Liu, X., 2022. Persistent late Permian to early Triassic warmth linked to enhanced reverse weathering. Nat. Geosci. 15, 832–838.

Cheng, C., Li, S., Xie, X., Cao, T., Manger, W.L., Busbey, A.B., 2019. Permian carbon isotope and clay mineral records from the Xikou section, Zhen'an, Shaanxi Province, Central China: Climatological implications for the easternmost Paleo-Tethys. Palaeogeogr. Palaeoclimatol. Palaeoecol. 514, 407–422.

Cleal, C.J., Thomas, B.A., 2005. Palaeozoic tropical rainforests and their effect on global climates: is the past the key to the present? Geobiology 3, 13–31.

Dal Corso, J., Song, H.J., Callegaro, S., Chu, D.L., Sun, Y.D., Hilton, J., Grasby, S.E., Joachimski, M.M., Wignall, P.B., 2022. Environmental crises at the Permian–Triassic mass extinction. Nat. Rev. Earth Environ. 3, 197–214.

Ernst, R.E., Youbi, N., 2017. How large Igneous Provinces affect global climate, sometimes cause mass extinctions, and represent natural markers in the geological record. Palaeogeogr. Palaeoclimatol. Palaeoecol. 478, 30–52.

Fedo, C.M., Nesbitt, H.W., Young, G.M., 1995. Unraveling the effects of potassiumme-tasomatism in sedimentary-rocks and paleosols, with implications for paleo-weathering conditions and provenance. Geology 23, 921–924.

Fielding, C.R., Frank, T.D., Birgenheier, L.P., Rygel, M.C., Jones, A.T., Roberts, J., 2008. Stratigraphic imprint of the Late Paleozoic Ice Age in eastern Australia: a record of alternating glacial and nonglacial climate regime. J. Geol. Soc. Lond. 165, 129–140.

Fielding, C.R., Frank, T.D., Birgenheier, L.P., 2023. A revised, late Palaeozoic glacial time-space framework for eastern Australia, and comparisons with other regions and events. Earth-Sci. Rev. 236, 104263.

Garbelli, C., Shen, S.Z., Immenhauser, A., Brand, U., Buhl, D., Wang, W.Q., Zhang, H., Shi, G.R., 2019. Timing of Early and Middle Permian deglaciation of the southern

hemisphere: Brachiopod-based ⁸⁷Sr/⁸⁶Sr calibration. Earth Planet. Sci. Lett. 516, 122–135.

Glasspool, I.J., Scott, A.C., 2010. Phanerozoic concentrations of atmospheric oxygen reconstructed from sedimentary charcoal. Nat. Geosci. 3, 627–630.

Glasspool, I.J., Edwards, D., Axe, L., 2004. Charcoal in the Silurian as evidence for the earliest wildfire. Geology 32 (5), 381–383.

Glasspool, I.J., Scott, A.C., Waltham, D., Pronina, N., Shao, L., 2015. The impact of fire on the Late Paleozoic Earth system. Front. Plant Sci. 6, 756.

Goddéris, Y., Donnadieu, Y., Carretier, S., Aretz, M., Dera, G., Macouin, M., 2017. Onset and ending of the late Palaeozoic ice age triggered by tectonically paced rock weathering. Nat. Geosci. 10, 382–386.

Goldberg, K., Humayun, M., 2010. The applicability the Chemical Index of Alteration as a paleoclimatic indicator: an example from the Permian of the Paraná Basin, Brazil. Palaeogeog. Palaeoclimatol. Palaeoecol. 293, 175–183.

Goodarzi, F., 1985. Optically anisotropic fragments in a Western Canadian subbituminous coal. Fuel 64, 1294–1300.

Grasby, S.E., Them, T.R., Chen, Z., Yin, R., Ardakani, O.H., 2019. Mercury as a proxy for volcanic emissions in the geologic record. Earth-Sci. Rev. 196, 102880.

Guo, Y., Bustin, R.M., 1998. FTIR spectroscopy and reflectance of modern charcoals and fungal decayed woods: implications for studies of inertinite in coals. Int. J. Coal Geol. 37, 29–53.

Isbell, J.L., Miller, M.F., Wolfe, K.L., Lenaker, P.A., Chan, M.A., Archer, A.W., 2003. Timing of late Paleozoic glaciation in Gondwana; was glaciation responsible for the development of Northern Hemisphere cyclothems? Special papers (Geological Society of America) 370, 5–24.

Jones, T.P., Lim, B., 2000. Extraterrestrial impacts of wildfires. Palaeogeog., Palaeoclimatol. Palaeoecol. 164 (5), 57–66.

Jones, B., Manning, D.A.C., 1994. Comparison of geochemical indices used for the interpretation of palaeoredox conditions in ancient mudstones. Chem. Geol. 111, 111–129.

Koch, J.T., Frank, T.D., 2012. Imprint of the late Palaeozoic Ice Age on stratigraphic and carbon isotopic patterns in marine carbonates of the Orogrande Basin, New Mexico, USA. Sedimentology 59, 291–318.

Korte, C., Jasper, T., Kozur, H.W., Veizer, J., 2005. δ¹⁸O and δ¹³C of Permian brachiopods: a record of seawater evolution and continental glaciation. Palaeogeog. Palaeoecol. 224, 333–351.

Liu, Y., Hu, Z., Gao, S., Günther, D., Xu, J., Gao, C., Chen, H., 2008. In situ analysis of major and trace elements of anhydrous minerals by LA-ICP-MS without applying an internal standard. Chem. Geol. 257, 34–43.

Lu, J., Wang, Y., Yang, M.F., Shao, L., Hilton, J., 2021a. Records of volcanism and organic carbon isotopic composition (δ¹³Corg) linked to changes in atmospheric pCO2 and climate during the Pennsylvanian icehouse interval. Chem. Geol. 570, 120168.

Lu, J., Wang, Y., Yang, M., Zhang, P., Bond, D.P.G., Shao, L., Hilton, J., 2022. Diachronous end-Permian terrestrial ecosystem collapse with its origin in wildfires. Palaeogeogr. Palaeoclimatol. Palaeoecol. 594, 110960.

Lu, J., Zhang, P.X., Dal Corso, J., Yang, M.F., Greene, S.E., Wignall, P.B., Lyu, D., Shao, L., Hilton, J., 2021b. Volcanically driven lacustrine ecosystem changes during the Carnian Pluvial Episode. Proc. Natl. Acad. Sci. U. S. A. 118 (40), e2109895118.

Lu, J., Zhou, K., Zhang, P.X., Yang, M.F., Shao, L., Hilton, J., 2021c. Continental records of organic carbon (δ13Corg) and volcanism linked to atmospheric pCO₂ and climate during the late Paleozoic Icehouse. Glob. Planet. Chang. 207, 103654.

Lv, D.W., Li, Z.X., Liu, H.Y., Guo, J.B., Liu, B.B., Meng, Z.L., 2009. Sea level change and sequence stratigraphy response of late Paleozoic in North China. Geol. China 36, 1079–1086.

McLennan, S.M., 1993. Weathering and global denudation. J. Geol. 101, 295–303.

Meyers, P.A., Lee, C., 1994. Preservation of elemental and isotopic source identification of sedimentary organic matter. Chem. Geol. 114, 289–302.

Montañez, I.P., Poulsen, C.J., 2013. The late paleozoic ice age: an evolving paradigm. Annu Rev Earth Pl Sc 41, 629–656.

Montañez, I.P., Tabor, N.J., Niemeier, D., DiMichele, W.A., Frank, T.D., Fielding, C.R., Isbell, J.L., Birgenheier, L.P., Rygel, M.C., 2007. CO₂-forced climate and vegetation instability during late Paleozoic deglaciation. Science 315, 87–91.

Murthy, S., Mendhe, V.A., Uhl, D., Mathews, R.P., Mishra, V.K., Gautam, S., 2021. Palaeobotanical and biomarker evidence for Early Permian (Artinskian) wildfire in the Rajmahal Basin, India. J. Palaeogeogr. 10, 5.

Nesbitt, H.W., Young, G.M., 1984. Prediction of some weathering trends of plutonic and volcanic rocks based on thermodynamic and kinetic considerations. Geochim. Cosmochim. Acta 48, 1523–1534.

Pattan, J.N., Pearce, N.J.G., Mislankar, P.G., 2005. Constraints in using Cerium-anomaly of bulk sediments as an indicator of paleo bottom water redox environment: a case study from the Central Indian Ocean Basin. Chem. Geol. 221, 260–278. https://doi.org/10.1016/j.chemgeo.2005.06.009.

Percival, L., Bergquist, B.A., Mather, T.A., Sanei, H., 2021. Sedimentary mercury enrichments as a tracer of large igneous province volcanism, large igneous provinces. American Geophysical Union 247–262.

Poulsen, C.J., Pollard, D., Montanez, I.P., Rowley, D., 2007. Late Paleozoic tropical climate response to Gondwanan deglaciation. Geology 35, 771–774.

Richey, J.D., Montañez, I.P., Goddéris, Y., Looy, C.V., Griffis, N.P., DiMichele, W.A., 2020. Influence of temporally varying weatherability on CO₂-climate coupling and ecosystem change in the late Paleozoic. Climates Past 16, 1759–1775.

Ross, C.A., Ross, J.R.P., 1987. Late Paleozoic Sea levels and depositional sequences. Cushman Found. Foraminifer. Res. Spec. Publ. 24, 137–149.

Roy, D.K., Roser, B.P., 2013. Climatic control on the composition of Carboniferous-Permian Gondwana sediments, Khalaspir basin, Bangladesh. Gond. Res. 23, 1163–1171.

Sanei, H., Grasby, S.E., Beauchamp, B., 2012. Latest Permian mercury anomalies. Geology 40, 63–66.

Sato, A.M., Llambías, E.J., Basei, M.A.S., Castro, C.E., 2015. Three stages in the late Paleozoic to Triassic magmatism of southwestern Gondwana, and the relationships with the volcanogenic events in coeval basins. J. S. Am. Earth Sci. 63, 48–69.

Scheffler, K., Hoernes, S., Schwark, L., 2003. Global changes during Carboniferous-Permian glaciation of Gondwana; linking polar and equatorial climate evolution by geochemical proxies. Geology 31, 605–608.

Scheffler, K., Buehmann, D., Schwark, L., 2006. Analysis of late Paleozoic glacial to postglacial sedimentary successions in South Africa by geochemical proxies—Response to climate evolution and sedimentary environment. Palaeogeog. Palaeoclimatol. Palaeoecol. 240, 184–203.

Scotese, C.R., 2014. Atlas of Permo-Triassic Paleogeographic Maps (Mollweide Projection), Volumes 3&4 of the Paleomap Atlas for ArcGIS, Paleomap Project, Evanston, IL. Tech. Rep. 3&4, 43–52.

Scott, A.C., 2010. Charcoal recognition, taphonomy and uses in palaeoenvironmental analysis. Palaeogeogr., Palaeoclimatol. Palaeoecol. 291, 11–39.

Shang, G., 1997. The Late Paleozoic Coal Geology of North China Platform. Shanxi Science and Technology Press, Taiyuan, pp. 1–160.

Shao, L., Wang, X., Wang, D., Li, M., Wang, S., Li, Y., Shao, K., Zhang, C., Gao, C., Dong, D., Cheng, A., Lu, J., Ji, C., Gao, D., 2020. Sequence stratigraphy, paleogeography, and coal accumulation regularity of major coal-accumulating periods in China. Int. J. Coal Sci. Technol. 7, 240–262.

Shellnutt, J.G., 2018. The Panjal Traps. Geol. Soc. Lond., Spec. Publ. 463, 59–86.

Shen, J., Feng, Q., Algeo, T.J., Liu, J., Zhou, C., Wei, W., Liu, J., Them, T.R., Gill, B.C., Chen, J., 2020a. Sedimentary host phases of mercury (Hg) and implications for use of Hg as a volcanic proxy. Earth Planet. Sci. Lett. 543, 116333.

Shen, J., Chen, J., Algeo, T.J., Feng, Q., Yu, J., Xu, Y., Xu, G., Lei, Y., Planavsky, N.J., Xie, S., 2020b. Mercury fluxes record regional volcanism in the South China craton prior to the end-Permian mass extinction. Geology 49, 452–456.

Shen, J., Chen, J., Zhang, S., Algeo, T.J., Bottjer, D.J., Yu, J., Xu, G., Penman, D., Wang, Y., Li, L., Shi, X., Planavsky, N.J., Feng, Q., Xie, S., 2022a. Intensified continental chemical weathering and carbon-cycle perturbations linked to volcanism during the Triassic–Jurassic transition. Nat. Commun. 13, 299.

Shen, J., Yin, R., Algeo, T.J., Svensen, H.H., Schoepfer, S.D., 2022b. Mercury evidence for combustion of organic-rich sediments during the end-Triassic crisis. Nat. Commun. 13.

Shen, J., Chen, J., Yu, J., Algeo, T.J., Smith, R.M.H., Botha, J., Frank, T.D., Fielding, C.R., Ward, P.D., Mather, T.A., 2023. Mercury evidence from southern Pangea terrestrial sections for end-Permian global volcanic effects. Nat. Commun. 14.

Sláma, J., Košler, J., Condon, D.J., Crowley, J.L., Gerdes, A., Hanchar, J.M., Horstwood, M.S., Morris, G.A., Nasdala, L., Norberg, N., 2008. Plešovice zircon - A new natural reference material for U–Pb and Hf isotopic microanalysis. Chem. Geol. 249, 1–35.

Sun, R., Yuan, J., Sonke, J.E., Zhang, Y., Zhang, T., Zheng, W., Chen, S., Meng, M., Chen, J., Liu, Y., Peng, X., Liu, C., 2020. Methylmercury produced in upper oceans accumulates in deep Mariana Trench fauna. Nat. Commun. 11, 3389.

Taylor, T.N., Taylor, E.L., Krings, M., 2009. Paleobotany: The Biology and Evolution of Fossil Plants (2nd Ed.). Academic Press (1252 pgs).

Them, T.R., Jagoe, C.H., Caruthers, A.H., Gill, B.C., Grasby, S.E., Gröcke, D.R., Yin, R., Owens, J.D., 2019. Terrestrial sources as the primary delivery mechanism of mercury to the oceans across the Toarcian Oceanic Anoxic Event (Early Jurassic). Earth Planet. Sci. Lett. 507, 62–72.

Thibodeau, A.M., Ritterbush, K., Yager, J.A., West, A.J., Ibarra, Y., Bottjer, D.J., Berelson, W.M., Bergquist, B.A., Corsetti, F.A., 2016. Mercury anomalies and the timing of biotic recovery following the end-Triassic mass extinction. Nat. Commun. 7, 11147.

Tierney, K.E., 2010. Carbon and Strontium Isotope Stratigraphy of the Permian from Nevada and China: Implications from an Icehouse to Greenhouse Transition. Doctoral dissertation.. The Ohio State University.

Vervoort, P., Adloff, M., Greene, S.E., Kirtland Turner, S., 2019. Negative carbon isotope excursions: an interpretive framework. Environ. Res. Lett. 14, 85014.

Wang, J., 2010. Late Paleozoic macrofloral assemblages from Weibei Coalfield, with reference to vegetational change through the late Paleozoic Ice-age in the North China Block. Int. J. Coal Geol. 83, 292–317.

Wiedenbeck, M., Hanchar, J.M., Peck, W.H., Sylvester, P., Valley, J., Whitehouse, M., Kronz, A., Morishita, Y., Nasdala, L., Fiebig, J., Franchi, I., Girard, J.P., Greenwood, R.C., Hinton, R., Kita, N., Mason, P.R.D., Norman, M., Ogasawara, M., Piccoli, P.M., Rhede, D., Satoh, H., Schulz-Dobrick, B., Skår, Ø., Spicuzza, M.J., Terada, K., Tindle, A., Togashi, S., Vennemann, T., Xie, Q., Zheng, Y.-F., 2004. Further characterisation of the 91500 zircon crystal. Geostand. Geoanal. Res. 28, 9–39.

Wu, Q., Ramezani, J., Zhang, H., Wang, J., Zeng, F., Zhang, Y., Liu, F., Chen, J., Cai, Y.F., Hou, Z.S., Liu, C., Yang, W., Henderson, C.M., Shen, S.Z., 2021. High-precision U-Pb age constraints on the Permian floral turnovers, paleoclimate change, and tectonics of the North China block. Geology 49, 677–681.

Xu, Y.G., Wei, X., Luo, Z.Y., Liu, H.Q., Cao, J., 2014. The early Permian Tarim large Igneous Province: Main characteristics and a plume incubation model. Lithos 204, 20–35.

Yager, J.A., West, A.J., Thibodeau, A.M., Corsetti, F.A., Rigo, M., Berelson, W.M., Bottjer, D.J., Greene, S.E., Ibarra, Y., Jadoul, F., Ritterbush, K.A., Rollins, N., Rosas, S., Di Stefano, P., Sulca, D., Todaro, S., Wynn, P., Zimmermann, L., Bergquist, B.A., 2021. Mercury contents and isotope ratios from diverse depositional environments across the Triassic–Jurassic Boundary: Towards a more robust mercury proxy for large igneous province magmatism. Earth-Sci. Rev. 223, 103775.

Yang, Y.J., Cawood, P.A., Du, Y.S., Feng, B., Yan, Y.J., 2014. Global continental weathering trends across the Early Permian glacial to postglacial transition; correlating high- and low-paleolatitude sedimentary records. Geology 42, 835–838.

Yin, R., Feng, X., Hurley, J.P., Krabbenhoft, D.P., Lepak, R.F., Hu, R., Zhang, Q., Li, Z., Bi, X., 2016. Mercury isotopes as proxies to identify sources and environmental impacts of mercury in sphalerites. Sci Rep-Uk 6, 18686.

Zeng, J., Cao, C.Q., Davydov, V.I., Shen, S.Z., 2012. Carbon isotope chemostratigraphy and implications of palaeoclimatic changes during the Cisuralian (early Permian) in the southern Urals, Russia. Gond. Res. 21, 601–610.

Zhang, H., Shen, G., He, Z., 1999. A carbon isotopic stratigraphic pattern of the late Palaeozoic coals in the North China platform and its paleoclimatic implications. Acta Geol. Sin. 73, 111–119.

Zhang, P., Yang, M., Lu, J., Shao, L., Wang, Z., Hilton, J., 2022. Low-latitude climate change linked to high-latitude glaciation during the late paleozoic ice age: evidence from terrigenous detrital kaolinite. Frontiers Earth Sci. 10 https://doi.org/10.3389/feart.2022.956861.